High Surface Area Porous Platinum Electrodes for Enhanced Charge Transfer

Yelin Hu[1,2], Aswani Yella[2], Stefan Guldin[3],
Francesco Stellacci[3], Michael Grätzel[2], Morgan Stefik[4*]

[1] Laboratory for High Performance Ceramics, Empa, Swiss Federal Laboratories for Materials Science and Technology, CH-8600 Dübendorf, Switzerland
[2] Laboratory of Photonics and Interfaces, Institute of Chemical Sciences and Engineering, Swiss Federal Institute of Technology, CH-1015 Lausanne, Switzerland
[3] Supramolecular Nanomaterials and Interfaces Laboratory, Institute of Materials, Swiss Federal Institute of Technology, CH-1015 Lausanne, Switzerland
[4] Department of Chemistry and Biochemistry, University of South Carolina, Columbia, South Carolina 29208, United States
*Corresponding author: morgan@stefikgroup.com

Abstract
Cobalt-based electrolytes are highly tunable and have pushed the limits of dye-sensitized solar cells, enabling higher open-circuit voltages and new record efficiencies. However, the performance these electrolytes and a range of other electrolytes suffer from slow electron transfer at platinum counter electrodes. High surface area platinum would enhance catalysis, but pure platinum structures are too expensive in practice. Here, we develop a material-efficient host-guest architecture that uses an ultrathin layer of platinum deposited upon an electrically conductive scaffold: niobium doped tin oxide (NTO). This nanostructured composite enhanced the counter electrode performance of DSCs using a $Co^{(II/III)}BPY_3$ electrolyte with an increased fill factor and power conversion efficiency (11.26%), as compared to analogous flat films. Our modular strategy was elaborated by integrating a light scattering layer onto the counter electrode to reflect unabsorbed light back to the photoanode to improve the short circuit current density and power conversion efficiency.

Introduction
In the past two decades, dye-sensitized solar cells (DSCs) have attracted considerable attention as a next generation of photovoltaic devices, due to their low cost, environmental friendliness, and simple preparation procedures. DSCs consist of three fundamental components[1]: a monolayer of adsorbed dye on a wide bandgap semiconductor as a working electrode, a hole transporting redox electrolyte, and a platinized counter electrode. Considerable effort has been devoted to improving the overall conversion efficiency by developing alternatives redox systems to replace the widely used I^-/I_3^- electrolytes. Cobalt based electrolytes have emerged as a promising and more tunable redox system[2]. Besides the reduced visible light absorption and improved chemical compatibility, cobalt-based redox shuttles show simpler kinetics and require a smaller energy expenditure for the dye regeneration process, thus improving the V_{OC}.[3] A 13% efficiency was achieved in DSCs with a $[Co(bpy)_3]^{2+/3+}$ based electrolyte in conjunction with a custom synthesized donor-π-bridge-acceptor zinc porphyrin (SM-315)[4]. Despite great advances, the catalysis of cobalt-based electrolytes on platinum counter electrodes remains challenging due to the slow charge-transfer kinetics at the cathode[5]. Stability is another crucial aspect for many applications where the noble metal status of platinum is significantly beneficial. Yet, a number of redox systems are only moderately catalyzed by platinum and would be much enhanced by having higher catalytic surface area.[6-10]

An approach to improve the charge transfer kinetics and minimize the overpotential losses from charge transfer reactions is to increase the active area of the counter electrodes by nanostructuring[1, 11]. However, a high surface area structure of pure platinum would greatly increase the materials costs. To this end, we present a host-guest strategy to efficiently use thin layers of platinum and enhance charge transfer to $Co^{2+/3+}$ electrolytes. The counter electrode fabrication starts with a colloidal film to provide high surface area and is followed by the atomic layer deposition (ALD) of conductive Nb doped SnO_2. The platinum catalyst is then uniformly deposited via ALD with a view towards optimal material utilization. This modular strategy was elaborated further by integrating a light scattering layer onto the composite counter electrode architecture to improve light management.

Results and Discussion

Platinum Catalyst Deposition and Characterization

The atomic layer deposition of Pt is limited by nucleation and starts as discrete clusters before proceeding to conformal film growth[12]. This presents a significant advantage since both the platinum nanoparticle size and surface area may be easily moderated via the number of ALD cycles. This is in stark contrast to other synthetic methods such as-thermal decomposition, electrodeposition, or electroless depostion[13]. In order to identify the optimum parameters in terms of morphology and electrochemical performance, a series of platinum catalyst thin films was prepared and studied on F:SnO$_2$ (FTO) substrates. Please note the surface roughness of the substrates is on the range of 1.5 to 3. A series of depositions was carried out with 10, 30, 50, 150 ALD cycles and the corresponding SEM images are shown in Fig. 1, indicating that discrete and well dispersed platinum nanoparticles were uniformly deposited on the surface. Instead of layer-by-layer growth, ALD deposited Pt grows in a nucleation limited fashion with dispersed particles initially and later extending to conformal film coatings [14].

The catalytic performance of the series of ALD "flat" Pt films were evaluated with electrochemical impedance spectroscopy (EIS) using a symmetric cell configuration. The directly on the substrate deposited films were named accordingly Pt-NTO-*X*, where *X* corresponds to the number of ALD cycles. The resulting Nyquist plots are shown in Fig. 2b and fit parameters are listed in Table I using a standard model (Fig. 2a). The Nyquist plots all exhibit a semi-circle corresponding to the charge transfer resistance at high frequencies, and a diagonal line with slope of 45° corresponding to the Warburg impedance from the electrolyte diffusion at low frequencies. A single Randle's circuit in series with a Warburg element was sufficient to obtain a good fitting. The diameter of the arc scales with the overall charge transfer resistance. The series resistance monotonically decreased with additional ALD cycles until a count of 50 ($R_{CT} = 25.3$ Ω cm^2), likely due to the increased platinum surface area as the particles grew (Fig. 1e). From 50 to 150 cycles, though, the charge transfer resistance increased, which we associate to decreased platinum surface area as the particles coalesced. This trend was confirmed by analysis of the constant-phase element ($CPE = T^{-1}(jw)^{-p}$) which provides information of active surface areas of counter electrode: a large CPE:T value represents high active surface area[15]. The CPE:T value monotonically increased up to 50 deposition cycles and then monotonically decreased with further deposition. The film texture also followed this trend, becoming less rough as the deposition progressed to high numbers of cycles (Fig 1a-d). In order to optimize material usage, we calculated the ratio of charge transfer conductance (inverse of R_{CT}) to pulse counts and deduced the catalytic efficacy normalized by the pulse count (Table I). The trend of pulse efficacy follows the same trend as R_{CT}, where 50 counts resulted in both, highest charge transfer conductance and most efficient utilization of platinum (Fig. 2c). Thus the optimum 50 Pt ALD cycles was used for the fabrication of electrodes with higher roughness factor. Indeed, similar analysis will benefit a variety of applications where efficient utilization of platinum is a critical factor to balance cost and performance.[16, 17]

Host-Guest Counter Electrodes

The principal challenges for improved performance of DSCs with cobalt electrolytes are to increase the fill factor and short circuit current density, J_{SC}. NTO-supported Pt films were prepared on colloidal templates ranging from 1 to 10 μm in thickness to access a range of different roughness factors (Table II). About 10 nm of NTO was coated onto the template to provide for electron transport to the FTO substrate, similar to our previous studies using ultrathin

layers for electron transport[18, 19]. The resulting NTO films are transparent (0.99 μm^{-1} at 550 nm), conductive (37 S/cm) and stable over a wide range of pH.[20]

The optimized 50 cycle deposition of Pt was deposited on top of the NTO host. SEM imaging of resulting composite nanostructure clearly show the rough platinum nanoparticle layer on top of the ~ 150 nm colloid-based architecture (Fig. 3a,b). XRD analysis of the composite films confirmed the presence of the anatase template, the crystalline tin oxide (cassiterite PDF# 41-1445) coating, and the platinum metal coating (PDF# 04-0802) (Fig. 3c). Scherrer analysis indicated an average grain size of 3-4 nm. A key feature of this architecture is the large ~200 nm-sized pores for facile diffusion of bulky cobalt electrolytes.

The catalytic performance of host-guest electrodes were investigated through EIS measurements of symmetric cells. The host-guest electrodes were named as 3D-Pt-NTO-X, where X represents the calculated roughness factor of the template. As shown in Table II, the R_{CT} values for host-guest electrodes ranged from 9.9 Ω cm^2 to 1.9 Ω cm^2 for roughness factors varying from 26 to 129 respectively, greatly improved from the value of 25.3 Ω cm^2 for flat Pt electrodes. This is consistent with the Nyquist plots shown in Fig. 4 where the semi-circles of electrodes 3D-Pt-NTO-26 to 3D-Pt-NTO-129 were smaller than that of the control electrode with a flat configuration, indicating faster reduction rates on host/guest counter electrodes. The CPE:T value increased for host-guest electrodes by a factor of 35 as compared to flat films, consistent with enhanced active surface area. Curiously, even rougher host-guest electrodes with a RF of 258 exhibited reduced charge transfer conductance (R_{CT}, 57.6 Ω cm^2). This deviation at high RF is attributed to ALD infiltration limitations into such thick TiO$_2$ films.

Relation Between Roughness Factor and Charge Transfer Resistance

The charge transfer resistance is affected by the configuration of the electrode. Han et al.[11] have found a linear dependence of charge transfer resistance on roughness factor. We found that the expected linear relationship between $\sigma_{CT}=1/R_{CT}$ and RF (Fig. 5a), clearly illustrating significantly improved charge transfer with rougher host-guest structures. Alongside, we expect a linear relationship between charge transfer conductance and roughness factor, which is presented as:

$$\sigma_{CT,3D} = \sigma_{CT,Pt}RF_{pt} \qquad (1)$$

where $\sigma_{CT,3D}$ is the charge transfer conductance of the host-guest structure, $\sigma_{CT,Pt}$ is the charge transfer conductance of a truly flat platinum film, and RF_{Pt} is the overall roughness factor of the platinum (area of platinum/projected area of electrode). It is important to note that RF_{Pt} is the product of both the host-guest roughness factor and the Pt ALD deposition roughness factor, RF_{ALD}, since the platinum deposition itself introduces additional roughness. However, these values are difficult to measure directly so we start analysis with the morphologic roughness factor RF_{3D} and use the best-fit data to back calculate RF_{Pt} and RF_{ALD}. The equation (1) may be rewritten as:

$$\sigma_{CT,3D} = \sigma_{CT,Pt}RF_{ALD}RF_{3D} \qquad (2)$$

. Plotting $\sigma_{CT,3D}$ versus RF_{3D} allows for a linear best-fit to be established with a significant Pearson's correlation coefficient of $r^2 = 0.987$ (Fig. 5a). The slope of 0.0039 gives a statistically significant relationship of $\sigma_{CT,Pt}$ to RF_{ALD}. Inserting this value into the above formula with RF_{3D} = 1.0 allows the extraction of:

$$\sigma_{CT,3D} = 0.004 = \sigma_{CT,Pt}RF_{ALD}$$

The value of $\sigma_{CT,Pt}$ may be estimated from the charge transfer conductance of the flattest ALD films (flat-150), resulting in RF_{ALD} of 2.65. It is important to note that this value yields some error due to the FTO roughness.

The tunable host-guest 3D-Pt architecture enabled high performance counter electrodes with a charge transfer resistance as low as 1.9 Ω cm^2. This low resistance is suitable for high performance DSC fabrication with improved fill factor and power conversion efficiency. The current density of a solar cell is a function of the total series resistance, and can be determined by the theoretical expression $I = I_{ph} - I_0 \left\{ exp \left[\dfrac{q\left(V+I\left(R_S+R_{diff}+R_{CT}\right)\right)}{nkT} \right] - 1 \right\} - \dfrac{V+I\left(R_S+R_{diff}+R_{CT}\right)}{R_{sh}}$, where, I_{ph} is the constant current source, I_0 is diode saturation current, q is elementary charge, V is voltage, n is ideality factor, k is Boltzmann constant, T is temperature, and R_{sh} is the shunt resistance.[21] Our *FF* estimation is based on a working area of 0.16 cm^2, an infinite shunt resistance, an I_{ph} of 17.3 mA/cm^2, and an I_0 of 3.28 × 10^{-13} A/cm^2. The ideality factor of the dye **YD2** was used (1.52)[2]. Based on the impedance results from Table II, and average sheet resistance (R_S) of 10 Ω was used. The diffusion resistance (R_{diff}) of dummy cells with a 70 μm electrolyte layer was around 70 Ω, resulting in R_{diff} of 11 Ω for a norm DSC with 11 μm electrolyte layer. Here, a linear relationship between diffusion resistance (R_{diff}) and the thickness of the electrolyte layer[11] The simulated *J-V* curves with charge transfer resistance of 1.9, 4, 10, 25 Ω cm^2, respectively, are shown in Fig. 5b. These calculations clearly show the effect of charge transfer resistance on DSC performance, where a charge transfer resistance of 1.9 Ω cm^2 is expected to result in a *FF* of 0.749.

Solar Cell Performance

The *J-V* characteristics for the optimized host-guest CEs are shown in Fig. 6 and table III. This data is compared to two other CEs: an analogous "flat" ALD platinum film prepared under the same conditions and a standard platinum electrode prepared from thermal reduction of H$_2$PtCl$_6$ (Fig. 6). Both of these reference counter electrodes used the same TEC 7 FTO glass with an identical NTO thin film. The host-guest sample had a roughness factor of 129, used the optimum 50 pulse cycles of platinum and had a charge transfer resistance of 1.9 Ω cm^2. All the DSCs were prepared with a 3.5 μm TiO$_2$ scattering layer on the anode in order to increase light scattering and improve light harvesting. The photovoltaic characteristics of the three DSCs are summarized in Table III, including the open-circuit voltage (V_{OC}), the short-circuit current (J_{SC}), fill factor (*FF*) and energy conversion efficiency (η). At 100% intensity, the DSC with 3D-Pt-NTO-129 counter electrode showed energy conversion efficiency of 11.26%, which is sgnificantly higher than the value of 3.7% and 9.91% obtained for the flat Pt-NTO and Pt(H$_2$PtCl$_6$)-NTO electrodes, as listed in Table III. Notably, the FF was improved for host-guest structures with 0.757 for 3D-Pt-NTO-129 as compared to 0.674 for Pt-NTO. Please note that the *Jsc* for Pt-NTO sample was limited by the counter electrode rather than the photoanode, reflected in a low power conversion efficiency coupled with a seemingly decent *FF*. If the saturation current density of Pt-NTO was higher, we would expect a much lower fill factor as illustrated in Fig. 5b. Under same illumination conditions, the V_{OC} values were all largely the same. Similarly, the J_{SC} values of the DSC with 3D-Pt-NTO-129 were slightly higher than Pt(H$_2$PtCl$_6$)-NTO and may be related to either light scattering off the counter electrode, or experimental error. The improved fill factors with the host-guest structure enabled the highest performance in these otherwise identical devices.

Elaboration of Host-Guest Electrode with a Light Scattering Layer

Our modular strategy is compatible with the placement of photonic structures such as scattering layers, 3D photonic crystals[22], bragg reflectors[22, 23], or optical metamaterials[24] above the optimized catalyst structure. Relocating the scattering layer from the anode to the cathode introduces several benefits such as simplifying the anode processing, reducing its pore tortuosity and alleviating diffusion constraints[25], as well as lowering its overall capacitance due to the large number of sub bandgap states in the excess TiO_2 volume. To demonstrate this concept, we added a ~7 μm thick TiO_2 scattering layer on top of the host-guest CE, shown in Fig. 7b. The double layer architectures exhibited a dramatically enhanced reflectivity, ranging from 65-80% in the spectral range of 700 to 400 nm. This compares to a total reflectance of around 10% for a counter electrode without a scattering layer. Thus, light that is transmitted through the photoanode will greatly be reflected back to the anode at high-angle and significantly increase the optical path length (Fig 7c). All optical measurements were performed with the electrodes infiltrated with acetonitrile to mimic the refractive index environment in functioning electrodes.

DSCs were fabricated both on the host-guest CE with and without the scattering layer. In both cases, a transparent 4 μm thick layer of ~20nm TiO_2 particles was used as the photoanode. The light scattering host-guest structure improved photocurrent and led to an 7% increase in the power conversion efficiency, from 8.6% to 9.2% (Fig. 8a). Though, the addition of the scattering layer led to a slight decrease in fill factor, from 0.783 to 0.761, likely due to the additional diffusion constraints for the electrolyte. Characterisation of the Incident-Photon-to-Charge-Carrier Efficiency (IPCE) confirmed the improved photocurrent with the structural elaboration, shown in Fig. 8b. The improved light harvesting was particularly evident with longer wavelengths from 550-650 nm that have weaker attenuation in the dye. The AM 1.5 photocurrent estimated by integrating the IPCE confirmed a significant improvement by 24.4%. Such counter electrodes with photon management are anticipated to improve the performance of a range of photoelectrodes such as Fe_2O_3 or Cu_2O used for solar water splitting.[26-28]

Conclusion

In summary, we demonstrate a material-efficient route to high surface area platinum counter electrodes by introducing a host-guest architecture. The host-guest electrodes exhibited improved charge transfer to electrolytes and with tunable performance by a factor of more than 4,000. The high performance electrodes were utilized in combination with cobalt-based electrolytes, enabled DSC fabrication with improved fill factor and enhanced energy-conversion efficiency of 11.26%. The structure was further elaborated to include a light scattering layer in the counter electrode, intended to return non-absorbed light back to the photoanode. This light scattering host-guest architecture improved the short circuit current density and power conversion efficiency. This approach is broadly applicable and anticipated to improve a range of photoelectrodes.

Materials and Methods

All reagents were used without further purification unless noted. Ethanol (98%) was obtained from Aldrich. Terpineol, acetonitrile (CAN, 99%) and tetrakis(diethylamino) Tin (TDMASn) were purchased from ABCR. The (tert-butylimino)tris(diethylamino) Niobium was obtained from Digital Specialty Chemicals (99.8%). The host template was prepared from ~200 nm TiO_2 particles: Tioxide A-HR (HUNTMAN Tioxide, 99.0% purity) using reported procedures[29].

Conductive fluorine doped tin oxide (FTO) with a sheet resistance of 7 Ω per square and 5% haze were supplied by Hartford Glass Co. The counter electrode substrates were cut into 3 x 3 cm^2 pieces. A sand-blaster was employed to drill holes in the glass for electrolyte back filling[29].

Prior to use, the FTO glass was subjected to ultrasonic cleaning using deconex surfactant and ethanol, and then heated to 450 °C.

Counter Electrode Preparation
Titania film was utilized as porous template and prepared from a TiO_2 paste, ethyl cellulose, and terpineol according to published procedures[29]. The thickness was controlled by adjusting the dilution of the TiO_2 paste as well as the spin coating speed and time.

ALD Depositions
All ALD depositions were carried out with a Cambridge NanoTech (Ultratech) Savannah 100 reactor. Niobium doped tin oxide was prepared as previously described in detail[20]. The resulting amorphous films were crystallized under flowing argon gas to 550 °C for 1 hour. Platinum was deposited from (Trimethyl)methylcyclopentadienyl platinum(IV) ($MeCpPtMe_3$) and oxygen gas precursors[12, 30]. The pulse cycle timing was 1/5/1/5 s for platinum/purge/oxygen/purge stages. The temperature in the deposition chamber was set to 250 °C and the platinum precursor was preheated to 75 °C. After platinum ALD, the films were heated to 510 °C in air to clean prior to cell fabrication.

Symmetric Cell Fabrication
The experimental setup for kinetic measurements of charge transfer resistance was a symmetric-cell, also known as a "dummy-cell".[31] Two identical platinized counter electrodes were sealed by a 70 μm-thick Surlyn film (Dupont) as a spacer with a fixed active area of 0.25 cm^2. The cell was filled with the same cobalt-based electrolyte used as the solar cell fabrication section described below.

Preparation of Mesoporous Photoanode Films
The screen printable TiO_2 paste was prepared as previously described. The mean particle size was around 20 nm with a pore diameter of 32 nm and porosity of 64%, as determined by N_2 physisorption. The paste was screen printed onto a pre-cleaned TCO glass (NSG 10, Nippon sheet glass, Japan) and pretreated with $TiCl_4$ (twice, 60 mM, 1hr at 80 °C), followed by a series of sintering steps (from ambient temperature to 125 °C (25 °C/min) - 10min hold - to 325 °C (13.3 °C/min) - 5 min hold - to 375 °C (10 °C/min) - 5 min hold - to 450 °C (15°C/min) - 15 min hold - to 500 °C (10°C/min) - 15 min hold). The thickness of the printed film after the sintering process was measured using a KLA Tencor alpha-step 500 surface profilometer and was found to be around 7 μm. The mesoporous TiO_2 photoanodes were post-treated with freshly prepared $TiCl_4$ solutions by immersing the substrates into a $TiCl_4$ bath at 70 °C for 30 min.

Solar Cell Fabrication
The photoanodes were sintered at 500 °C for 30 minutes prior to dipping them in the 0.2 mM dye solution in 1/4 (v/v) THF/Ethanol mixture for 6 hours. The sensitized electrodes were then washed in acetonitrile to remove any loosely bound dye molecule aggregates before the cell assembly. The counter electrodes were prepared as mentioned above. The two electrodes were melt sealed using a 25 μm thick Surlyn hotmelt-ionomer (Dupont, USA) film. The electrolyte used was an acetonitrile solution of 250 mM Co^{2+}, 60 mM Co^{3+}, 100 mM LiTFSI and 200 mM 4-tert-butyl pyridine. The electrolyte was introduced into the cell by a vacuum back filling technique through a hole sand-blasted at the side of the counter electrodes.

Scanning Electron Microscopy

The morphology of the samples was characterized via top-view and cross-section using a Zeiss Merlin scanning electron microscope (SEM) with a field emission source and an accelerating voltage of 5 kV. An in-lens detector measured secondary electrons.

Roughness Factor Determination

The roughness factor of prepared the titania templates was estimated based on the equation[32]: $RF = P \times \rho \times S \times d$, where RF is the roughness factor (active surface area/projected area), P is porosity, ρ is the density of powder, S is the specific surface area, and d is the thickness of films. A bulk density value of 3.85 g/cm^3 was used for anatase, and the specific surface area was 10.55 m^2/g determined by BET adsorption-desorption experiments. The porosity then was calculated by weighing a film of known volume. A scaled-up titania film (10 × 15 cm) was fabricated in an identical process, and the average thickness was measured by surface profilopmetry after a series of calcinations. The film was then scraped and weighed to yield a calculated porosity of 63.6%.

Reflectivity Spectra

The reflectivity of the counter electrodes before and after the integration of a scattering layer was characterized by an integrating sphere with a diameter of 8 inches and a barium sulfate-based coating (Oriel, model 70679). In order to mimic the optical media in the device, the porous electrodes were infiltrated by acetonitrile. The scattering signal was collected with a high sensitivity spectrometer (Ocean Optics, QE65000) and normalized by the reflectance of a Lambertian reference surface. An optical trap was used for the deduction of the specular reflection.

X-ray Diffractometer (XRD)

A Bruker D8 Discover diffractometer with monochromatic Cu Kα1 radiation (1.540598 Å) was used for X-ray diffraction. The scattered X-rays were acquired via a standard two-theta mode by moving the source and linear silicon strip "Lynx Eye" detector through the angular range.

Electrochemical Impedance Spectroscopy (EIS)

Electrochemical impedance spectroscopy measurements were carried out with the Eco-Chimie Autolab PGSTAT 10 with FRA module. The measured frequency range was 10 mHz to 100kHz with a 10 mV amplitude perturbation. The obtained data were fitted to an equivalent circuit using Zview software (Scribner Associates).

Photovoltaic Characterization

A 450 W xenon lamp (Oriel, USA) was used as a solar simulator for photovoltaic (J-V) characterizations. The spectral output of the lamp was manipulated with Schott K113 Tempax sunlight filter (Präzisions Glas & Optik GmbH, Germany) to reduce the mismatch between the simulated and actual solar spectrum to less than 2 %. The *J-V* characteristics of the cells were recorded with a Keithley model 2400 digital source meter (Keithley, USA). The photoactive area of 0.159 cm^2 was defined using a blackened metal mask.

References

[1]   N. Papageorgiou, *Coord. Chem. Rev.* **2004**, 248, 1421.

[2]   A. Yella, H.-W. Lee, H. N. Tsao, C. Yi, A. K. Chandiran, M. K. Nazeeruddin, E. W.-G. Diau, C.-Y. Yeh, S. M. Zakeeruddin, M. Grätzel, *Science* **2011**, 334, 629.

[3]   Y. Liu, J. R. Jennings, Y. Huang, Q. Wang, S. M. Zakeeruddin, M. Grätzel, *The Journal of Physical Chemistry C* **2011**, 115, 18847.

[4]   S. Mathew, A. Yella, P. Gao, R. Humphry-Baker, F. E. CurchodBasile, N. Ashari-Astani, I. Tavernelli, U. Rothlisberger, K. NazeeruddinMd, M. Grätzel, *Nat Chem* **2014**, advance online publication.

[5]   P. J. Cameron, L. M. Peter, S. M. Zakeeruddin, M. Grätzel, *Coordination Chemistry Reviews* **2004**, 248, 1447.

[6]   J.-H. Yum, E. Baranoff, F. Kessler, T. Moehl, S. Ahmad, T. Bessho, A. Marchioro, E. Ghadiri, J.-E. Moser, C. Yi, M. K. Nazeeruddin, M. Grätzel, *Nat Commun* **2012**, 3, 631.

[7]   E. Reddington, A. Sapienza, B. Gurau, R. Viswanathan, S. Sarangapani, E. S. Smotkin, T. E. Mallouk, *Science* **1998**, 280, 1735.

[8]   U. A. Paulus, T. J. Schmidt, H. A. Gasteiger, R. J. Behm, **2001**, 495.

[9]   R. M. Rioux, H. Song, J. D. Hoefelmeyer, P. Yang, G. A. Somorjai, *The Journal of Physical Chemistry B* **2004**, 109, 2192.

[10]   M. Schneider, D. G. Duff, T. Mallat, M. Wildberger, A. Baiker, *J. Catal.* **1994**, 147, 500.

[11]   L. Han, N. Koide, Y. Chiba, A. Islam, R. Komiya, N. Fuke, A. Fukui, R. Yamanaka, *Appl. Phys. Lett.* **2005**, 86, 213501.

[12]   T. Aaltonen, M. Ritala, T. Sajavaara, J. Keinonen, M. Leskelä, *Chem. Mat.* **2003**, 15, 1924.

[13]   A. Kloke, F. von Stetten, R. Zengerle, S. Kerzenmacher, *Adv. Mater.* **2011**, 23, 4976.

[14]   S. Sun, G. Zhang, N. Gauquelin, N. Chen, J. Zhou, S. Yang, W. Chen, X. Meng, D. Geng, M. N. Banis, R. Li, S. Ye, S. Knights, G. A. Botton, T.-K. Sham, X. Sun, *Sci. Rep.* **2013**, 3.

[15]   V.-D. Dao, S.-H. Kim, H.-S. Choi, J.-H. Kim, H.-O. Park, J.-K. Lee, *The Journal of Physical Chemistry C* **2011**, 115, 25529.

[16]   B. C. H. Steele, A. Heinzel, *Nature* **2001**, 414, 345.

[17]   C. He, S. Desai, G. Brown, S. Bollepalli, *The Electrochemical Society Interface* **2005**, 41.

[18]   M. Stefik, M. Cornuz, N. Mathews, T. Hisatomi, S. Mhaisalkar, M. Grätzel, *Nano Lett.* **2012**, 12, 5431.

[19]   A. K. Chandiran, A. Yella, M. Stefik, L.-P. Heiniger, P. Comte, M. K. Nazeeruddin, M. Graetzel, *Acs Applied Materials & Interfaces* **2013**, 5, 3487.

[20]   M. Stefik, M. Cornuz, N. Mathews, T. Hisatomi, S. Mhaisalkar, M. Gratzel, *Nano Letters* **2012**, 12, 5431.

[21]   S. M. Sze, *Physics of Semiconductor Devices*, John Wiley & Sons, **1981**.

[22]   A. Mihi, H. Míguez, *The Journal of Physical Chemistry B* **2005**, 109, 15968.

[23]   S. Guldin, M. Kolle, M. Stefik, R. Langford, D. Eder, U. Wiesner, U. Steiner, *Adv. Mater.* **2011**, 23, 3664.

[24]   S. Vignolini, N. A. Yufa, P. S. Cunha, S. Guldin, I. Rushkin, M. Stefik, K. Hur, U. Wiesner, J. J. Baumberg, U. Steiner, *Adv. Mater.* **2012**, 24, OP23.

[25]   S. Guldin, S. Hüttner, M. Kolle, M. E. Welland, P. Müller-Buschbaum, R. H. Friend, U. Steiner, N. Tétreault, *Nano Lett.* **2010**, 10, 2303.

[26]   S. C. Riha, B. M. Klahr, E. C. Tyo, S. Seifert, S. Vajda, M. J. Pellin, T. W. Hamann, A. B. F. Martinson, *ACS Nano* **2013**.

[27]   S. D. Tilley, M. Schreier, J. Azevedo, M. Stefik, M. Graetzel, *Adv. Funct. Mater.* **2014**, 24, 303.

[28]   A. Paracchino, N. Mathews, T. Hisatomi, M. Stefik, S. D. Tilley, M. Gratzel, *Energy & Environmental Science* **2012**, 5, 8673.

[29]   S. Ito, T. N. Murakami, P. Comte, P. Liska, C. Grätzel, M. K. Nazeeruddin, M. Grätzel, *Thin Solid Films* **2008**, 516, 4613.

9

[30]   S. T. Christensen, J. W. Elam, F. A. Rabuffetti, Q. Ma, S. J. Weigand, B. Lee, S. Seifert, P. C. Stair, K. R. Poeppelmeier, M. C. Hersam, M. J. Bedzyk, *Small* **2009**, 5, 750.
[31]   A. Hauch, A. Georg, *Electrochim. Acta* **2001**, 46, 3457.
[32]   K. Kalyanasundaram, *Dye-sensitized Solar Cells*, EFPL Press, **2010**.
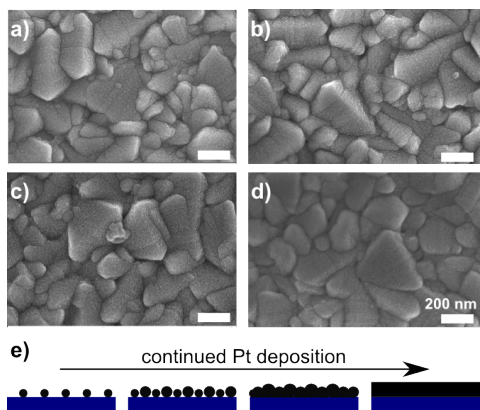
Figure 1. SEM top-view of platinum films conformally coated with atomic layer deposition onto NTO conducting substrates using (a) 10, (b) 30, (c) 50 or (d) 150 pulse sequences, respectively. (e) Schematic of Pt growth during ALD deposition. Note that the large ~200 nm features correspond to the FTO structure beneath the ~10nm thick NTO.
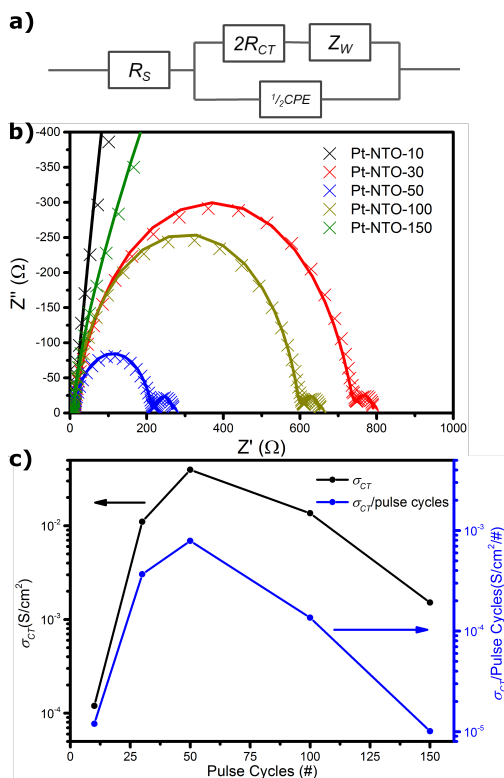

Figure 2. (a) Circuit model used to fit (b) Nyquist diagram of symmetric cells prepared with ALD Pt deposited onto "flat" NTO-coated FTO as a function of the number of Pt pulse cycles, from 10-150. (c) Dependence of charge transfer conductance of Pt-

NTO films with pulse count (black) and the ratio of charge transfer conductance to pulse counts (blue). The Nyquist plots show measured points and solid best-fit curves.

Table I. Fit parameters for EIS data of Pt-NTO counter electrodes

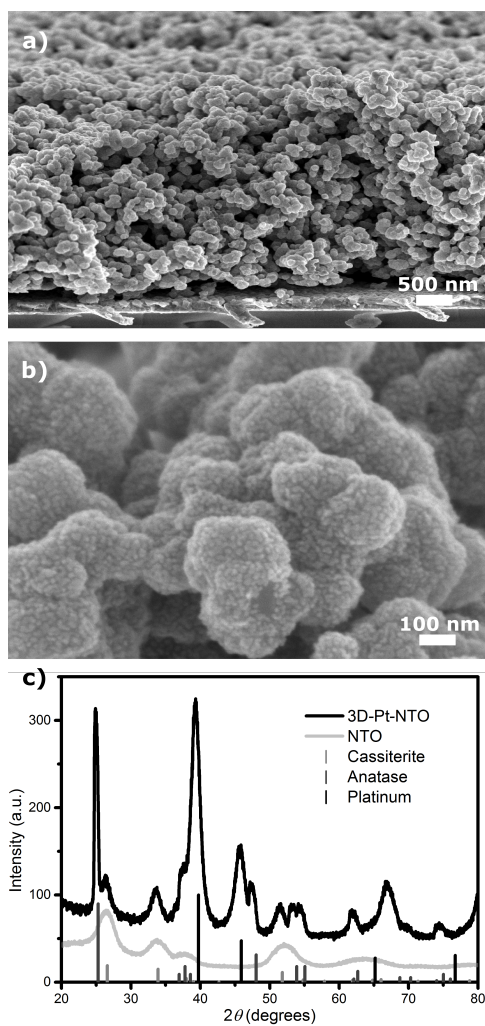|	σ_{ct}/Pulse (S/cm^2)	R_S (Ω)	R_{CT} (Ω cm^2)	CPE: T (F cm^{-2})	CPE: P	Z_W: R (Ω s$^{-0.5}$)	Z_W: T (s)	Z_W: P
Pt-NTO-10	1.20E-05	11.3	8362.2	3.6e-6	1.00	14185	0.89	0.5
Pt-NTO-30	3.68E-04	10.6	90.5	1.1e-5	0.88	56.18	5.69	0.5
Pt-NTO-50	7.91E-04	10.0	25.3	1.2e-5	0.88	55.71	5.55	0.5
Pt-NTO-100	1.36E-04	8.7	73.3	2.2e-7	0.91	55.59	4.60	0.5
Pt-NTO-150	1.01E-05	8.2	661.5	1.1e-5	0.91	123.7	1.30	0.5

Figure 3. (a, b) SEM images and (c) X-ray diffraction patterns of host-guest 3D-Pt-NTO (black). The XRD reference pattern for NTO on a quartz substrate (light gray) is shown as well as the allowed reflections for cassiterite (gray), anatase (dark gray), and platinum (black).
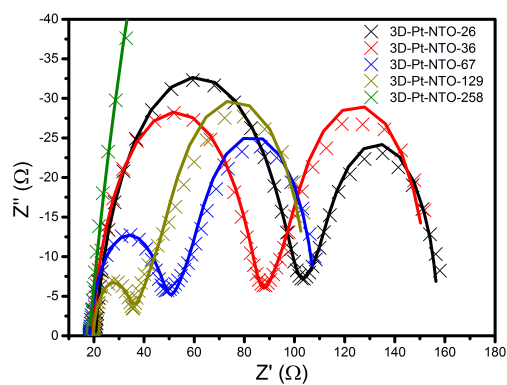
Figure 4. Nyquist plots for host-guest 3D-Pt-NTO counter electrodes with different template roughness factors, from 26-258. Measured points and solid best-fit curves are shown.

Table II. Fit parameters for EIS data of 3D-Pt-NTO counter electrodes

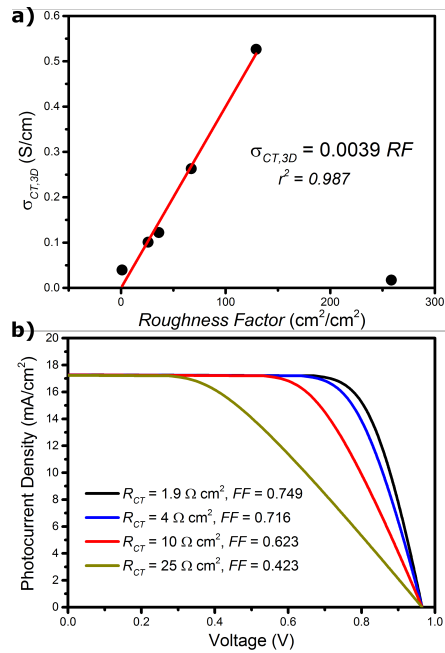|	d (μm)	Roughness factor	R_S (Ω)	R_{CT} (Ω cm²)	CPE: T (F cm⁻²)	CPE: P	Z_W : R (Ω s⁻⁰·⁵)	Z_W : T (s)	Z_W : P
3D-Pt-NTO-26	1	25.8	20.6	9.9	8.2e-5	0.87	57.58	5.77	0.5
3D-Pt-NTO -36	1.4	36.2	19.6	8.2	8.0e-5	0.91	69.38	10.45	0.5
3D-Pt-NTO -67	2.6	67.2	18.2	3.8	2.5e-4	0.87	60.04	7.22	0.5
3D-Pt-NTO -129	5	129.2	17.8	1.9	4.2e-4	0.90	70.99	9.30	0.5
3D-Pt-NTO -258	10	258.4	18.2	57.6	7.8e-6	0.83	258.6	10.83	0.5

Figure 5. (a) Direct scaling of the charge transfer conductance with the host roughness factor. (b) Simulated *J-V* curves show the dependence of fill factor, FF, on different charge transfer resistances, R_{CT}. The calculated curves were based on a photocurrent of 17.3 mA/cm^2, a saturation current of 3.28×10^{-13} A/cm^2, an ideality factor of 1.52, an active area of 0.16 cm^2 and an infinite shunt resistance.
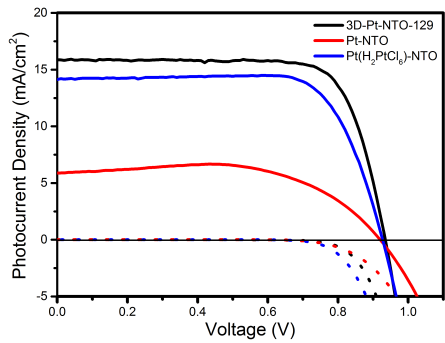

Figure 6. Current-voltage curves of DSCs fabricated using 3D-Pt-NTO-129 (black) compared with Pt-NTO counter electrodes (red) and standard Pt cathodes prepared on NTO, Pt(H$_2$PtCl$_6$)-NTO (blue). Solid lines indicate *J-V* characteristics under simulated AM 1.5 sunlight (100 mW/cm^2) and dashed lines show the dark current.

Table III. Performance parameters for DSCs with different cathodes

Counter electrode	Intensity (*sun*)	V_{OC} (V)	J_{SC} (mA cm^{-2})	*FF*	η (%)
Pt-NTO	98.5%	919	5.88	0.674	3.70
Pt-NTO	51.2%	879	4.74	0.501	4.08
Pt-NTO	9.5%	799	1.43	0.554	6.61
3D-Pt-NTO-129	99.8%	934	15.87	0.757	11.26
3D-Pt-NTO-129	51.1%	908	8.34	0.777	11.52
3D-Pt-NTO-129	9.7%	840	1.61	0.790	11.03
Pt(H_2PtCl_6)-NTO	98.9%	926	14.12	0.75	9.91
Pt(H_2PtCl_6)-NTO	50.9%	892	7.98	0.751	10.51
Pt(H_2PtCl_6)-NTO	9.5%	809	1.53	0.798	10.38

Table IV. Performance parameters for DSCs with and without scattering layer integrated on ALD 3D-Pt-NTO-129 counter electrodes

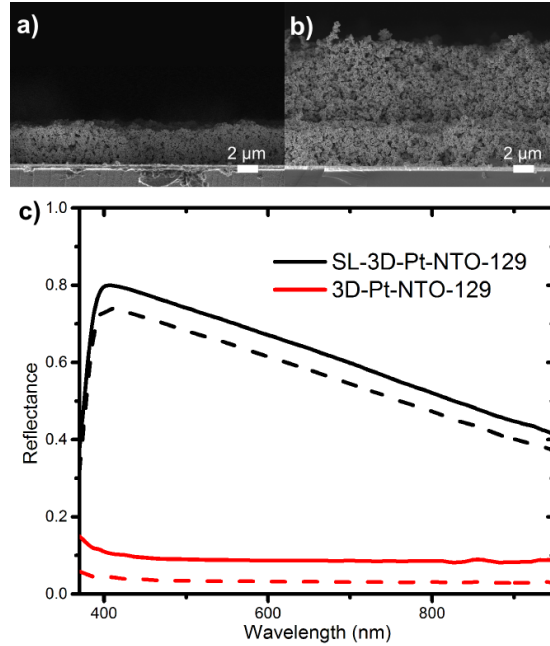| Counter electrode	Intensity *(sun)*	V_{OC} (V)	J_{SC} (mA cm^{-2})	*FF*	η (%)
3D-Pt-NTO-129	98.3%	904	11.96	0.783	8.61
3D-Pt-NTO-129	50.3%	874	6.40	0.781	8.68
3D-Pt-NTO-129	9.6%	800	1.22	0.80	8.22
SL-3D-Pt-NTO-129	98%	901	13.61	0.761	9.22
SL-3D-Pt-NTO-129	50.8%	871	7.03	0.767	9.25
SL-3D-Pt-NTO-129	9.5%	798	1.34	0.796	8.97

Figure 7. Cross-sectional SEM images of 3D-Pt-NTO-129 counter electrode (a) before and (b) after integrating a light scattering layer (SL-3D-Pt-NTO-129). (c) Comparison of total (solid) and diffused (dash) reflectance as measured with acetonitrile in the pores using an integrating sphere.
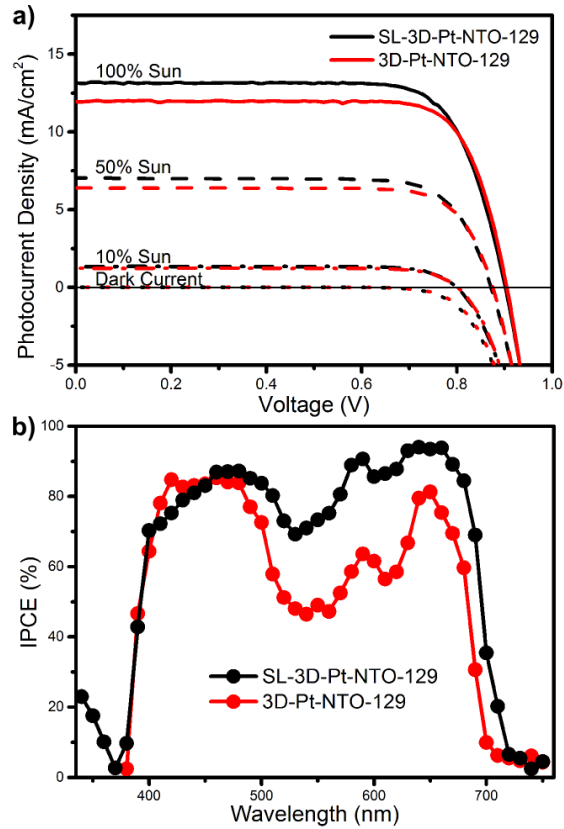

Figure 8. (a) Current-voltage curves and (b) incident photo to current conversion efficiency (IPCE) spectra of DSCs using 3D-Pt-NTO-129 and SL-3D-Pt-NTO-129 after integrating a light scattering layer.

15